

BEM–FEM coupling for the analysis of flexible propellers in non-uniform flows and validation with full-scale measurements

Maljaars, P. J.; Grasso, N.; den Besten, J. H.; Kaminski, M. L.

DOI

[10.1016/j.jfluidstructs.2020.102946](https://doi.org/10.1016/j.jfluidstructs.2020.102946)

Publication date

2020

Document Version

Accepted author manuscript

Published in

Journal of Fluids and Structures

Citation (APA)

Maljaars, P. J., Grasso, N., den Besten, J. H., & Kaminski, M. L. (2020). BEM–FEM coupling for the analysis of flexible propellers in non-uniform flows and validation with full-scale measurements. *Journal of Fluids and Structures*, 95, Article 102946. <https://doi.org/10.1016/j.jfluidstructs.2020.102946>

Important note

To cite this publication, please use the final published version (if applicable). Please check the document version above.

Copyright

Other than for strictly personal use, it is not permitted to download, forward or distribute the text or part of it, without the consent of the author(s) and/or copyright holder(s), unless the work is under an open content license such as Creative Commons.

Takedown policy

Please contact us and provide details if you believe this document breaches copyrights. We will remove access to the work immediately and investigate your claim.

BEM-FEM coupling for the analysis of flexible propellers in non-uniform flows and validation with full-scale measurements

P.J. Maljaars ¹, N. Grasso ², J.H. den Besten ¹, M.L. Kaminski ¹

¹ *Delft, University of Technology, Maritime & Transport Technology Department, Delft, The Netherlands*

² *Maritime Research Institute Netherlands, Wageningen, The Netherlands*

Abstract

The first part of the paper presents a partitioned fluid-structure interaction (FSI) coupling for the non-uniform flow hydro-elastic analysis of highly flexible propellers in cavitating and non-cavitating conditions. The chosen fluid model is a potential flow solved with a boundary element method (BEM). The structural sub-problem has been modelled with a finite element method (FEM). In the present method, the fully partitioned framework allows one to use another flow or structural solver. An important feature of the present method is the time periodic way of solving the FSI problem. In a time periodic coupling, the coupling iterations are not performed per time step but on a periodic level, which is necessary for the present BEM-FEM coupling, but can also offer an improved convergence rate compared to a time step coupled method. Thus, it allows to solve the structural problem in the frequency domain, meaning that any transients, which slow down the convergence process, are not computed. As proposed in the method, the structural equations of motion can be solved in modal space, which allows for a model reduction by involving only a limited number of mode shapes.

The second part of the paper includes a validation study on full-scale. For the full-scale validation study a purposely designed composite propeller with a diameter of 1 m has been manufactured. Also an underwater measurement set-up including a stereo camera system, remote control of the optics and illumination system has been developed. The propeller design and the underwater measurement set-up are described in the paper. During sea trials blade deflections have been measured in three different positions. A compari-

son between measured and calculated torque shows that the measured torque is much larger than computed. This is attributed to the differences between effective and nominal wakefields, where the latter one has been used for the calculations. To correct for the differences between measured and computed torque the calculated pressures have been amplified accordingly. In that way the deformations which have been computed with the BEM-FEM coupling for non-uniform flows became very similar to the measured results.

Keywords: flexible marine propellers, fluid-structure interaction, numerical modelling, full-scale validation

1. Introduction

Over the last decades many papers have been published on the hydro-elastic analysis of flexible (composite) propellers. The majority of studies have been limited to steady inflow conditions. Fewer papers have been published about the hydro-elastic analysis in behind ship conditions, i.e. involving non-uniform flows, for instance [1, 2, 3, 4]. The most probable reason for this is that the non-uniform flow conditions complicate the analyses significantly. First of all, the hydro-elastic analysis needs to be performed with the structural dynamic equations, a quasi-static analysis does not suffice [5]. This means that hydrodynamic damping and fluid added mass effects have to be incorporated in the analysis. For composite propellers the ratio between fluid added mass and structural mass will be much higher than one [5]. Computations with high fluid added mass ratios are prone to instabilities [6, 7] and therefore either a monolithic method has to be adopted, in which the fluid and structural problem are solved simultaneously, or a dedicated partitioning between fluid and structural solver is required to stabilize the coupling iterations between the two sub-domains.

A second complicating factor due to the non-negligible hydrodynamic damping and fluid added mass effects is that structural blade vibration velocities and accelerations have to be coupled to the fluid as well, whereas for uniform flow calculations only the blade deformations matter. Two different approaches have been presented in literature to cope with this. In [1, 2, 3, 4] the vibration-induced pressures have been written in terms of closed form expressions for added mass and hydrodynamic damping and moved to the left-hand side of the structural equations. The advantage of this approach is that the vibration induced pressures are directly included in the structural

analysis, resulting in a faster convergence. However, the derivation of the closed form expressions has been based on several assumptions, with the small blade deformation assumption as the most important one [5]. A more precise approach would be to include the vibration velocities and accelerations of the propeller blade by additional boundary conditions in the flow calculation. In [5] both approaches have been compared. It was concluded that the first approach provides reasonable results, because the structural response was dominated by stiffness and therefore the consequences of modelling errors in the fluid added mass and hydrodynamic damping contributions were relatively small. The second approach is recommended for problems involving significant blade deformations, i.e. highly flexible blades.

This paper is divided in two parts. The purpose of the first part is to present a fluid structure interaction (FSI) method for the hydro-elastic analysis of highly flexible blades in behind ship conditions. Since the kind of monolithic method as presented in [4] is limited to small deformations and extension of this method to large blade deformations seems hardly possible, a partitioned method has been adopted. An advantage of a partitioned method is that for the structural and fluid sub-problem existing black-box solvers can be used. In this work a boundary element method (BEM) for the fluid simulations has been used, but the present method may be suitable for other flow solvers as well. A BEM was chosen because this method is particularly effective in capturing the flow details but requires only 1% of the effort needed for fully viscous flow simulations [8]. In this work the BEM PROCAL, developed by the Maritime Research Institute Netherlands (MARIN) [9, 10], has been used. In PROCAL cavitation models have been implemented. Hence, the present method can be applied for the (non-)uniform flow FSI analysis of highly flexible blades, showing large blade deformations, in cavitating and non-cavitating conditions.

The second part of the paper shows a validation of the method with full-scale measurement results. In so far as literature presents results on the validation of flexible propeller calculations, those studies are for small-scale propellers (maximum diameter around 60 cm), where the measurement results are obtained from laboratory tests [11, 12, 13, 14, 15]. Except in [15] results for non-uniform flow conditions have been shown. For this work, full-scale tests have been performed with a purposely designed 1 m diameter glass-epoxy propeller. The full displacement field of the blades at the wake peak have been obtained with a digital image correlation technique. The measurement results have been compared to calculation results.

This work has been structured as follows: Section 2 presents the unsteady BEM-FEM coupling procedure. Section 3 explains the design of full-scale composite propeller. In Section 4 the full-scale measurement set-up has been explained. Section 5 provides a comparison of numerical and experimental results. Conclusions and recommendations are given in Section 6.

2. Unsteady BEM-FEM coupling procedure

The unsteady coupling procedure to compute the steady-state fluid structure interaction (FSI) response of flexible propellers in behind ship conditions (i.e. in a non-uniform flow) will be discussed in the following, starting with some background knowledge on FSI, a brief description of fluid and structural modelling and finally explaining the coupling scheme.

2.1. Fluid-structure interaction

2.1.1. Monolithic and partitioned FSI

Monolithic or partitioned methods can be used to solve FSI problems. In a monolithic method the fluid and structure problem are simultaneously solved using a single code. This might be difficult to realize because fluid and structural solvers are usually completely different each using its own optimized tools specific for the field of application. Furthermore, a monolithic solver might be very inefficient since structural and fluid problems are often solved differently (linearly and non-linearly) and with different temporal resolutions. However, in a monolithic scheme both fields have to be integrated with the highest of the two temporal resolutions. Another option is a partitioned method in which the fluid and structure problem are solved in separate codes. In case of strong interaction between fluid and structure, a partitioned method requires coupling iterations to converge to the monolithic solution, which can be computationally expensive. An important advantage of such a partitioning for the present method is that the structural problem may be coupled to a black-box fluid solver able to model cavitation as well. That was also an important reason to adopt a partitioned method for this work.

2.1.2. Time step and time periodic partitioned FSI

In a time step FSI coupling, fluid and structural calculations are alternately performed for each time step. In case of one fluid and structural evaluation for each time step, a time step difference exists between fluid and

structural solution. Then, for strongly coupled FSI problems, sub-iterations between fluid and structural solver are required to reach dynamic equilibrium for each time instant.

In case of a periodic FSI problem, the periodicity can be used to get rid of the time step difference by using results from the same time step of a previous period. This coupling is called the time periodic coupling and has been described and investigated in previous work [16]. A time periodic coupling is the most obvious for the present work for several reasons. First of all, the time periodic coupling can take advantage of the periodic nature of the problem to be solved. Secondly, the potential flow solver PROCAL used in this work is completely periodical in nature. Think of the vortex wake shedding and the use of symmetry blades [9] and therefore a non-periodic solution could not be treated in PROCAL. The time periodic coupling allows for first letting PROCAL to converge before new disturbances enter the equations.

An appealing advantage of the time periodic coupling is that it allows to solve for the structural equations in the frequency domain. That means that only the steady state response is obtained and any transients, which slow down the convergence to the steady state FSI solution, are not computed [16]. However, as shown, convergence problems as appearing in time step couplings due to strong fluid added mass effects, arise in time periodic couplings as well. This requires a dedicated partitioned solution method.

2.1.3. Partitioned solution methods

In a partitioned FSI method fluid and structural problems are separately solved and the coupling between the two sub-domains is accomplished by imposing boundary interface conditions. In that case a partitioned solution method has to be provided in which it is defined how the body boundary interface information has to be exchanged between the two solvers. Especially in case of a high ratio between fluid added mass and structural mass and an incompressible fluid, the solution process may not converge without a dedicated partitioned solution method [6]. Two of these partitioned solution methods have been investigated in a time step and time periodic framework in [16]. It has been shown that the Quasi-Newton inverse least squares (QN-ILS) method outperforms the Aitken under-relaxation method in any case. Furthermore, the QN-ILS method in a time periodic framework converges for any fluid added mass ratio. Therefore, in this work the QN-ILS method is applied in the unsteady coupling procedure for flexible propellers. For more results obtained with the QN-ILS partitioned solution method, the imple-

mentation of this method in a time-periodic framework and its convergence behaviour one is referred to [16]. Details on the mathematical background of the QN-ILS method can be found in [17].

2.2. Fluid model description

In this work the boundary element method (BEM) PROCAL has been used. PROCAL has been developed by the Maritime Research Institute Netherlands (MARIN) for the Cooperative Research Ships (CRS) to analyse the hydrodynamics of (non-)cavitating ship propellers in open-water and in behind ship conditions [9, 10]. In order to determine the fluid forces for flexible propellers in behind-ship conditions several modifications to PROCAL have been made in order to include deformation induced fluid velocities and accelerations. Due to blade deformations panel normal vectors become time-dependent, which is reflected in the panel source strengths. The hydrodynamic influence coefficients of the blade also become time-dependent. Finally, the pressures and fluid forces have to be evaluated from the computed velocity potentials on a modified grid. PROCAL has been modified to make it suitable for shape adaptive propeller modelling.

In [5] two different approaches to include blade deformation effects in BEM have been proposed. Both were implemented in PROCAL. In the partially geometry dependent (PGD) BEM modelling the source strengths are calculated from the blade deformation dependent panel normal vectors and the pressures and forces are evaluated on the modified BEM geometry, while keeping blade and wake influence coefficients constant. In the fully geometry dependent (FGD) BEM modelling, blade and wake influence coefficients are blade deformation dependent as well. This requires a significant amount of additional calculation time since the system of equations have to be recalculated for every time step. The results obtained with the PGD-BEM model are close to results obtained with FGD-BEM model. Although, it has been shown that some results obtained for the most flexible case with the PGD-BEM model do not comply with the accuracy criteria. Therefore, applying this modelling approach for very flexible cases needs to be considered carefully [5].

In the FGD-BEM modelling the total disturbance velocity potential Φ is solved with PROCAL. The total velocity, \mathbf{v} , relative to the operating propeller becomes,

$$\mathbf{v}(\mathbf{x}, t) = \mathbf{v}_0(\mathbf{x}, t) + \nabla\Phi(\mathbf{x}, t) \quad (1)$$

with \mathbf{v}_0 the inflow velocity, t the time and \mathbf{x} the position vector in a Cartesian coordinate system. The velocity, \mathbf{v}_0 , can be written as the sum of the ship's effective wake field velocity, \mathbf{v}_w , and the effect of the propeller angular velocity, $\boldsymbol{\theta}$,

$$\mathbf{v}_0(\mathbf{x}, t) = \mathbf{v}_w(\mathbf{x}, t) - \boldsymbol{\theta} \times \mathbf{x} \quad (2)$$

The flow is assumed to be incompressible and have a constant density. Therefore, Laplace's equation applies to the disturbance velocity potential,

$$\nabla^2 \Phi(\mathbf{x}, t) = 0 \quad (3)$$

Then, the fluid pressures, p , are related to the total velocity and the disturbance velocity potential according to Bernoulli's law,

$$\frac{\partial \Phi}{\partial t} + \frac{1}{2} |\mathbf{v}|^2 + \frac{p}{\rho} + gz = \frac{p_{ref}}{\rho} + \frac{1}{2} |\mathbf{v}_0|^2 \quad (4)$$

For a propeller, p_{ref} is the pressure far upstream (along the shaft axis) and it obeys the hydrostatic law, $p_{ref} = p_{atm} + \rho g z_{shaft}$, with p_{atm} the atmospheric pressure at the free surface, and the submergence z at the shaft being z_{shaft} . In order to solve Eq. 3 boundary conditions have to be imposed on the propeller surface, S_B and wake sheet, S_W , which contains the shed vorticity. On the propeller surface the impermeability condition is imposed for a deforming and vibrating blade,

$$\nabla \Phi \cdot \mathbf{n}(\mathbf{x}, \boldsymbol{\delta}) = -\mathbf{v}_0 \cdot \mathbf{n}(\mathbf{x}, \boldsymbol{\delta}) + \frac{\partial \boldsymbol{\delta}}{\partial t} \cdot \mathbf{n}(\mathbf{x}, \boldsymbol{\delta}) \quad (5)$$

The right hand side of this boundary condition consists of two parts, the surface normal velocity due to the inflow velocity, $\mathbf{v}_0 \cdot \mathbf{n}(\mathbf{x}, \boldsymbol{\delta})$, where the surface normal vector is also a function of blade deformation, $\boldsymbol{\delta}$. The second part, $\frac{\partial \boldsymbol{\delta}}{\partial t} \cdot \mathbf{n}(\mathbf{x}, \boldsymbol{\delta})$, is the vibration velocity of the deformed blade itself.

A relation between the disturbance potential on the fluid boundary surface and the source strengths (normal component of the disturbance velocity at the body boundary) for an unsteady flow and deformable body is given by the following integral equation [5],

$$\begin{aligned} 2\pi \Phi(\mathbf{a}(\boldsymbol{\delta}), t) = & \int_{S_B(\boldsymbol{\delta})} \left[\Phi(\mathbf{b}(\boldsymbol{\delta}), t) \frac{\partial G(\mathbf{a}(\boldsymbol{\delta}), \mathbf{b}(\boldsymbol{\delta}))}{\partial \mathbf{n}_b(\boldsymbol{\delta})} - \frac{\partial \Phi(\mathbf{b}(\boldsymbol{\delta}), t)}{\partial \mathbf{n}_b(\boldsymbol{\delta})} G(\mathbf{a}(\boldsymbol{\delta}), \mathbf{b}(\boldsymbol{\delta})) \right] dS \\ & + \int_{S_W(\boldsymbol{\delta})} \Delta \Phi(\mathbf{b}(\boldsymbol{\delta}), t) \frac{\partial G(\mathbf{a}(\boldsymbol{\delta}), \mathbf{b}(\boldsymbol{\delta}))}{\partial \mathbf{n}_b(\boldsymbol{\delta})} dS \end{aligned} \quad (6)$$

This integral equation follows from Morino’s formulation of Green’s third identity [18] and the dynamic boundary condition on the wake sheet. In this equation \mathbf{a} and \mathbf{b} are points on the fluid domain boundary surface and \mathbf{n}_b is the outward normal at \mathbf{b} . The Green’s function, G , for the Laplace equation is defined as,

$$G(\mathbf{a}, \mathbf{b}) = \frac{1}{r(\mathbf{a}, \mathbf{b})} \quad r(\mathbf{a}, \mathbf{b}) = |\mathbf{r}| = |\mathbf{a} - \mathbf{b}| \quad (7)$$

The integral equation Eq. 6 is solved in PROCAL by approximating the surfaces S_B and S_W by N_{total} panels. On each panel a collocation point is defined where the integral equation is applied. Finally, a system of equations is obtained, unknown in the strengths of the source and dipole elements. The system of equations is updated every time step according to the deformations in blade geometry and blade vibration velocities. For more details about the FGD-BEM modelling approach one is referred to [5].

2.3. Structure model description

Details about geometry and material aspects in the FEM modelling of composite ship propellers have been given in [19]. This subsection reveals the structural dynamic equations for a propeller blade and the analyses of dry and wet blade natural frequencies and mode shapes required for the structural analyses with a reduced model in modal space.

2.3.1. Propeller blade structural equations

For the case of a propeller in behind ship condition the structural dynamic equations for a propeller blade in a blade fixed (i.e. rotating) reference system is given by,

$$[\mathbf{M}_s] \{\ddot{\mathbf{u}}\} + [\mathbf{C}_s] \{\dot{\mathbf{u}}\} + [\mathbf{K}_s] \{\mathbf{u}\} = \{\mathbf{f}_h\} + \{\mathbf{f}_{fict}\} \quad (8)$$

where $[\mathbf{M}_s]$, $[\mathbf{C}_s]$ and $[\mathbf{K}_s]$ denote structural mass, damping and stiffness matrices. $\{\mathbf{f}_h\}$ is the hydrodynamic force vector, which implicitly includes fluid added mass, hydrodynamic damping and fluid stiffness contributions. The vector $\{\mathbf{f}_{fict}\}$ represents the fictitious forces as a result of solving a rotating problem in a body fixed reference system.

2.3.2. Loads

The hydrodynamic pressures are computed with the FGD-BEM model as explained in Section 2.2. Analyses are performed only for constant angular speeds which means that Euler forces are zero but centrifugal forces and Coriolis forces are present. The centrifugal force on a mass m rotating with angular velocity $\dot{\boldsymbol{\theta}}$ at position \mathbf{p} is,

$$\mathbf{f}_{centrifugal} = m \left(\dot{\boldsymbol{\theta}} \times \left(\dot{\boldsymbol{\theta}} \times \mathbf{p} \right) \right) \quad (9)$$

The Coriolis force is equal to,

$$\mathbf{f}_{Coriolis} = 2m \left(\dot{\boldsymbol{\theta}} \times \frac{d\mathbf{p}}{dt} \right) \quad (10)$$

The Coriolis force contributes to the total damping but is assumed to be negligible in comparison to the hydrodynamic damping and therefore neglected in the analyses [3]. Hence, only the centrifugal forces contribute to the fictitious force vector in Eq. 8.

2.3.3. Dry natural frequencies and eigenmodes

For an N degree of freedom structural system with mass matrix, $[\mathbf{M}]$, and stiffness matrix, $[\mathbf{K}]$, the structural dynamic equation for forced vibration is,

$$[\mathbf{M}] \{\ddot{\mathbf{u}}\} + [\mathbf{K}] \{\mathbf{u}\} = \{\mathbf{f}\} \quad (11)$$

where $\{\ddot{\mathbf{u}}\}$ and $\{\mathbf{u}\}$ are the structural acceleration and deformation vectors and $\{\mathbf{f}\}$ is the force vector. The natural frequencies $\omega_{i=1\dots N}$ and corresponding modes $\boldsymbol{\psi}_{i=1\dots N}$ follow from the solution of the eigenvalue problem,

$$[-\omega^2 \mathbf{M} + \mathbf{K}] \{\mathbf{u}\} = \{\mathbf{0}\} \quad (12)$$

The eigenmodes are orthogonal with respect to the system mass and stiffness matrix. This property can be utilized to transform the system of equations to the modal space. An uncoupled system of equations is obtained and the degrees of freedom are the modal participation factors, q_i , rather than the nodal structural response vectors. The first step in this transformation is to write the structural deformation vector as a linear combination of all the

eigenmodes,

$$\{\mathbf{u}\} = \sum_{i=1}^N \boldsymbol{\psi}_i q_i = [\boldsymbol{\Psi}] \{\mathbf{q}\} \quad (13)$$

$$[\boldsymbol{\Psi}] = [\boldsymbol{\psi}_1, \boldsymbol{\psi}_2, \dots, \boldsymbol{\psi}_N] \quad (14)$$

$$\{\mathbf{q}\} = \begin{bmatrix} q_1 \\ q_2 \\ \vdots \\ q_N \end{bmatrix} \quad (15)$$

Substituting these expressions in the structural dynamic equations and multiplying by $[\boldsymbol{\Psi}]^T$ gives,

$$[\boldsymbol{\Psi}]^T [\mathbf{M}] [\boldsymbol{\Psi}] \{\ddot{\mathbf{q}}\} + [\boldsymbol{\Psi}]^T [\mathbf{K}] [\boldsymbol{\Psi}] \{\mathbf{q}\} = [\boldsymbol{\Psi}]^T \{\mathbf{f}\} \quad (16)$$

When the modes are normalized with respect to the mass matrix, i.e. $[\boldsymbol{\Psi}]^T [\mathbf{M}] [\boldsymbol{\Psi}] = [\mathbf{I}]$, the following uncoupled system of equations is obtained,

$$[\mathbf{I}] \{\ddot{\mathbf{q}}\} + [\boldsymbol{\Omega}] \{\mathbf{q}\} = [\boldsymbol{\Psi}]^T \{\mathbf{f}\} \quad (17)$$

where $[\mathbf{I}]$ is the identity matrix and $[\boldsymbol{\Omega}]$ is a diagonal matrix with the square of the natural frequencies ω_i on its main diagonal.

2.3.4. Wet natural frequencies and eigenmodes

From the closed form expression for the fluid added mass matrix as presented in [5] a full non-symmetrical added mass matrix can be obtained. To calculate the wet natural frequencies and mode shapes the added mass matrix has to be added to the structural mass matrix. A possible approach is to lump the off-diagonal terms of the added mass matrix on its main diagonal and add it to the structural mass matrix in order to compute wet natural frequencies and mode shapes by solving the corresponding eigenvalue problem [3]. An important reason for this lumping is that many of the commercial FEM software packages cannot handle non-symmetric and non-sparse matrices.

To avoid lumping of the fluid added mass matrix and adding of the fluid added mass contribution by discrete masses in a black-box FEM solver the wet natural frequencies and mode shapes can be computed directly from dry frequencies and mode shapes and the fluid added mass matrix by the

following approach. First of all, the modal added mass matrix, $[\mathbf{\Gamma}]$, has to be computed from the full and non-symmetrical added mass matrix $[\mathbf{M}_h]$. In order to obtain a fully uncoupled system of equations, the modal added mass matrix needs to be symmetric. A symmetric modal added matrix, $[\mathbf{\Gamma}]$, has been obtained in the following way,

$$[\mathbf{\Gamma}] = [\mathbf{\Psi}]^T [\mathbf{M}_h^*] [\mathbf{\Psi}] \quad (18)$$

where $[\mathbf{M}_h^*] = \frac{1}{2} \left([\mathbf{M}_h] + [\mathbf{M}_h]^T \right)$. The symmetric modal added mass matrix is added to the structural modal mass matrix $[\mathbf{I}]$. In order to obtain the wet natural frequencies and mode shapes a second eigenvalue problem has to be solved in analogy with Eq. 12,

$$[-\bar{\omega}^2 [\mathbf{I} + \mathbf{\Gamma}] + \mathbf{\Omega}] \{\mathbf{q}\} = \{\mathbf{0}\} \quad (19)$$

From this eigenvalue problem the wet natural frequencies $\bar{\omega}_{i=1\dots N}$ and eigenvectors $\boldsymbol{\theta}_{i=1\dots N}$ are obtained. The eigenvectors $\boldsymbol{\theta}_i$ are eigenmodes in modal space. These eigenmodes are mass normalized with the total modal mass matrix $[\mathbf{I} + \mathbf{\Gamma}]$. The wet mode shapes are obtained by multiplying the matrix with the dry mode shapes by the eigenvector matrix $[\mathbf{\Theta}]$,

$$[\bar{\Psi}] = [\mathbf{\Psi}] [\mathbf{\Theta}] \quad (20)$$

where $[\mathbf{\Theta}] = [\boldsymbol{\theta}_1, \boldsymbol{\theta}_2, \dots, \boldsymbol{\theta}_N]$. Then, the wet modal stiffness matrix, $[\bar{\mathbf{\Omega}}]$, is equal to $[\mathbf{\Theta}]^T [\mathbf{\Omega}] [\mathbf{\Theta}]$ and is a diagonal matrix with the squared wet natural frequencies $\bar{\omega}_i$ on its main diagonal.

2.4. Coupling scheme

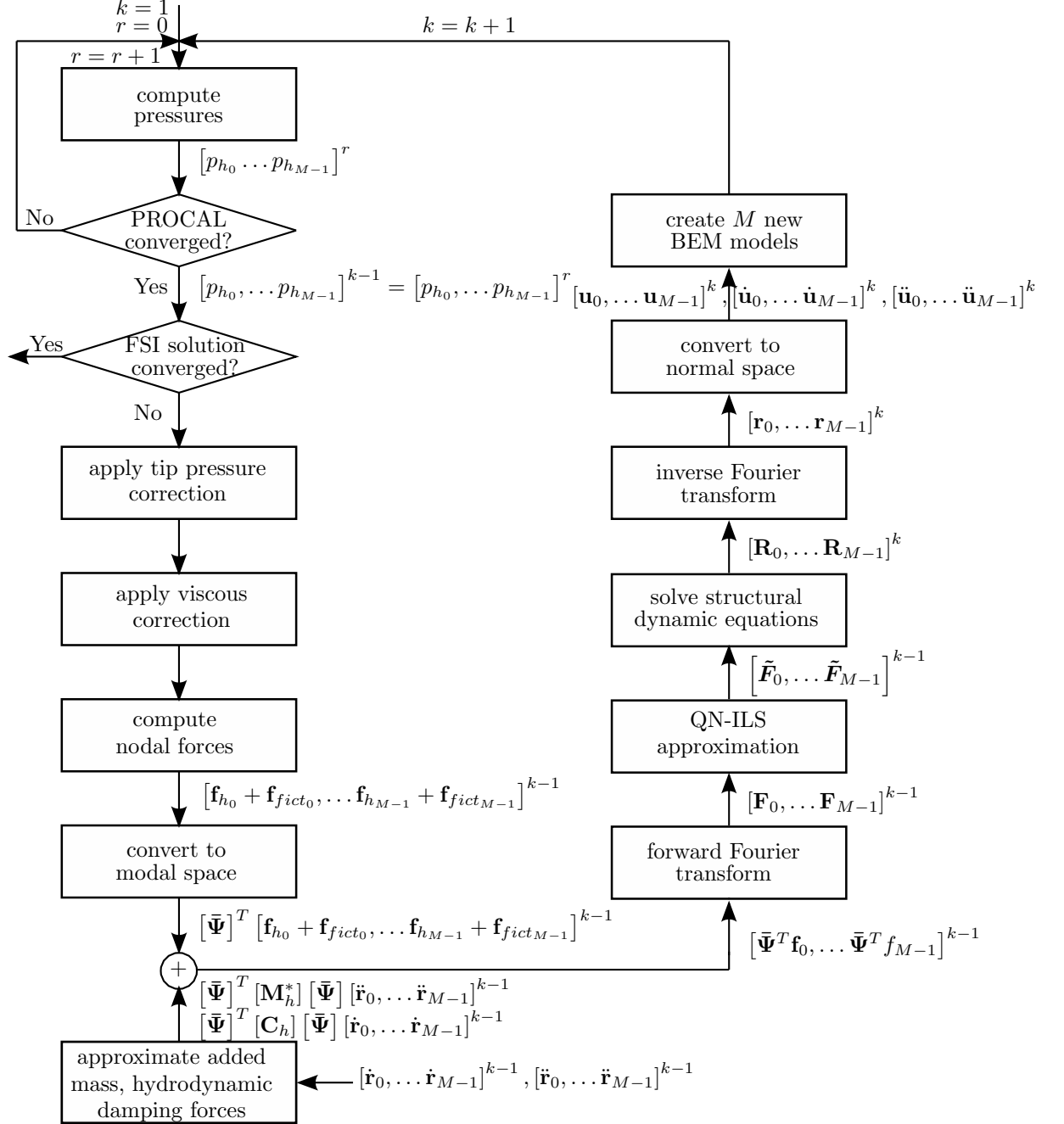


Figure 1: Flow chart of coupling scheme.

Figure 1 presents schematically the FSI coupling procedure. In this scheme index r is the counter of the number of PROCAL revolutions and index k is the counter of the number of FSI cycles. Generally, r will be larger than k since PROCAL requires an iterative procedure over a number of propeller revolutions in order to converge to a steady state flow solution. A propeller revolution is subdivided in M number of time steps. At the beginning of the first PROCAL calculation the indices k and r are one. The coupling scheme will be explained step by step in the following subsections.

2.4.1. Pressure calculation

The coupling scheme starts by computing with PROCAL the steady state solution for the loads on the undeformed propeller in the unsteady wakefield. As mentioned before, PROCAL solves this problem iteratively and therefore after every propeller revolution, r , the convergence to the steady state solution is checked. The converged hydrodynamic pressures for the full revolution at FSI cycle, k , are denoted with superscript $k - 1$ since in the PROCAL calculation the structural response of the previous FSI cycle has been used. After the PROCAL analysis the convergence of the FSI solution is monitored by comparing the hydrodynamic loads of the present and previous FSI cycle. When the load difference between these two cycles is smaller than a specified tolerance, the FSI solution is said to be converged, otherwise the calculation continues with two pressure corrections. The first correction is for the overestimation of the pressures at the propeller tip obtained with the BEM. The second one is a viscous correction for frictional losses. Both are explained in more detail in [20].

2.4.2. Loads

Once the pressures have been computed, they are imposed on the FEM model and the corresponding equivalent nodal forces are calculated together with the equivalent nodal forces of the centrifugal load. With the wet modes the loads for a full revolution are converted to wet modal space. Important to note is that identical meshes have been used in the BEM and FEM model [20]. The main advantage is that no interpolation of pressures and structural response is required in the exchange of boundary interface information between the fluid and structural domain.

2.4.3. Structural equations in wet modal space

For a better convergence, estimates for fluid added mass and hydrodynamic damping forces have been added to left- and right-hand side of the structural dynamic equation. Then, Eq. 8 for FSI cycle k reads,

$$([\mathbf{M}_s] + [\mathbf{M}_h^*]) \{\ddot{\mathbf{u}}\}^k + ([\mathbf{C}_s] + [\mathbf{C}_h]) \{\dot{\mathbf{u}}\}^k + [\mathbf{K}_s] \{\mathbf{u}\}^k = \{\mathbf{f}_h\}^{k-1} + \{\mathbf{f}_{fict}\}^{k-1} + [\mathbf{M}_h^*] \{\ddot{\mathbf{u}}\}^{k-1} + [\mathbf{C}_h] \{\dot{\mathbf{u}}\}^{k-1} \quad (21)$$

where $[\mathbf{C}_h]$ denotes the hydrodynamic damping matrix. The derivation of added mass and hydrodynamic damping matrices has been elaborated in [5] Eq. 21 shows clearly the main drawback of a partitioned method; the structural response for FSI cycle k is computed from the loads based on the previous FSI cycle $k - 1$.

The structural problem is solved in wet modal space. Accordingly, Eq. 21 transforms to,

$$[\bar{\Psi}]^T ([\mathbf{M}_s] + [\mathbf{M}_h^*]) [\bar{\Psi}] \{\ddot{\mathbf{r}}\}^k + [\bar{\Psi}]^T ([\mathbf{C}_s] + [\mathbf{C}_h]) [\bar{\Psi}] \{\dot{\mathbf{r}}\}^k + [\bar{\Psi}]^T [\mathbf{K}_s] [\bar{\Psi}] \{\mathbf{r}\}^k = [\bar{\Psi}]^T [\mathbf{M}_h^*] [\bar{\Psi}] \{\ddot{\mathbf{r}}\}^{k-1} + [\bar{\Psi}]^T [\mathbf{C}_h] [\bar{\Psi}] \{\dot{\mathbf{r}}\}^{k-1} + [\bar{\Psi}]^T (\{\mathbf{f}_h\} + \{\mathbf{f}_{fict}\})^{k-1} \quad (22)$$

which can be written as,

$$[\mathbf{I}] \{\ddot{\mathbf{r}}\}^k + [\bar{\mathbf{Z}}] \{\dot{\mathbf{r}}\}^k + [\bar{\mathbf{\Omega}}] \{\mathbf{r}\}^k = [\bar{\Psi}]^T \{\mathbf{f}\}^{k-1} \quad (23)$$

where $[\bar{\mathbf{Z}}]$ is the total damping matrix in wet modal space. After this transformation a weak coupling in the system of equations still exists as a result of the full hydrodynamic damping matrix, $[\mathbf{C}_h]$. This coupling in the system of equations has been neglected and model reduction has been applied by computing the modal participation factors only for a limited number of mode shapes.

The flow chart of Figure 1 shows that the added mass and hydrodynamic damping forces are approximated based on the response of the previous FSI cycle and are added to the other excitation forces, resulting in modal forces for the M times steps of a full revolution $[\bar{\Psi}^T \mathbf{f}_0, \bar{\Psi}^T \mathbf{f}_1, \dots, \bar{\Psi}^T \mathbf{f}_{M-1}]$.

2.4.4. Fourier transform

The time periodic coupling allows one to solve the structural problem in the frequency domain by taking advantage of the periodicity in the problem, resulting in a faster convergence to the steady state solution than in

case of solving the problem in the time domain [16]. With the forward Fourier transform the sequence of modal force vectors for a full revolution $[\bar{\Psi}^T \mathbf{f}_0, \bar{\Psi}^T \mathbf{f}_1, \dots, \bar{\Psi}^T \mathbf{f}_{M-1}]$ transform into M spectral components in the frequency domain, $[\mathbf{F}_0, \mathbf{F}_1 \dots \mathbf{F}_{M-1}]$, which are defined by,

$$\{\mathbf{F}_m\} = \sum_{l=0}^{M-1} [\bar{\Psi}]^T \{\mathbf{f}_l\} e^{-im\hat{\omega}t_l} \quad m = 0, 1, \dots, M-1 \quad (24)$$

where $\hat{\omega}$ is the fundamental frequency equal to $2\pi n$ in rad/s with n the propeller revolution rate in Hz. The inverse transform is then,

$$\{\bar{\Psi}^T \mathbf{f}_l\} = \sum_{m=0}^{M-1} \{\mathbf{F}_m\} e^{im\hat{\omega}t_l} \quad l = 0, 1, \dots, M-1 \quad (25)$$

2.4.5. QN-ILS approximation

By computing the structural response for each FSI cycle straight from Eq. 23 the FSI solution will blow up because of the strong coupling between fluid and structure. Therefore, a dedicated partitioned solution method is required to keep the iterative solution process stable and to converge to the steady state FSI solution in an efficient way. The method which has been implemented in this work is the Quasi-Newton inverse least squares (QN-ILS) method which belongs to the class of matrix-free Krylov subspace methods. Within the coupling method the frequency domain wet modal forces $\{\mathbf{F}\}^{k-1}$ might be used as an approximation for $\{\mathbf{F}\}^k$. Repeating this for subsequent FSI cycles is basically a Gauss-Seidel iterative way of solving the FSI problem, which does not necessarily (efficiently) converge. With the QN-ILS method a better approximation for $\{\mathbf{F}\}^k$ is made based on all previous iterates of $\{\mathbf{F}\}$ instead of simply using the last one, i.e. $\{\mathbf{F}\}^{k-1}$. The basic idea behind the QN-ILS approximation is that the best approximation for $\{\mathbf{F}\}^k = \{\tilde{\mathbf{F}}\}^{k-1}$, where $\{\tilde{\mathbf{F}}\}^{k-1}$ is that linear combination of $\{\mathbf{F}\}$ from previous iterates $\{k-1, k-2, \dots, 0\}$ that will minimise the residuals of the FSI solution [16, 21].

2.4.6. Frequency domain solution in wet modal space

Similar to the modal forces the time domain discretised wet modal participation factors \mathbf{r}_l are related to the wet modal participation factors in the

frequency domain \mathbf{R}_m by,

$$\{\mathbf{r}_l\} = \sum_{m=0}^{M-1} \{\mathbf{R}_m\} e^{im\hat{\omega}t} \quad l = 0, 1, \dots, M-1 \quad (26)$$

Eq. 23 can be written with the Fourier transformed QN-ILS approximated modal forces, $\{\tilde{\mathbf{F}}_m\}$, and wet modal participation factors, $\{\mathbf{R}_m\}$ as,

$$(-[\mathbf{I}]m^2\hat{\omega}^2 + i[\bar{\mathbf{Z}}]m\hat{\omega} + [\bar{\mathbf{\Omega}}]) \{\mathbf{R}_m\}^k e^{im\hat{\omega}t} = \{\tilde{\mathbf{F}}_m\}^{k-1} e^{im\hat{\omega}t} \quad (27)$$

The wet modal participation factors can be solved for $m = 0, \dots, M-1$ using,

$$\{\mathbf{R}_m\}^k = (-[\mathbf{I}]m^2\hat{\omega}^2 + i[\bar{\mathbf{Z}}]m\hat{\omega} + [\bar{\mathbf{\Omega}}])^{-1} \{\tilde{\mathbf{F}}_m\}^{k-1} \quad m = 0, 1, \dots, M-1 \quad (28)$$

2.4.7. Time domain solution in normal space

Having computed the sequence of M wet modal participation factors in the frequency domain, the next step is to convert the solution to the time domain. The time domain wet modal participation factors $\{\mathbf{r}_l\}$ can be obtained from the inverse Fourier transform of Eq. 26. In analogy with Eq. 13 the time domain nodal deformations can be obtained from the wet mode shapes and the wet modal participation factors,

$$\{\mathbf{u}_l\} = [\bar{\mathbf{\Psi}}] \{\mathbf{r}_l\} \quad l = 0, 1, \dots, M-1. \quad (29)$$

2.4.8. BEM model updating

Based on the structural response calculated for FSI cycle k , M new BEM models are constructed for the next FSI cycle. First of all, the new BEM models include the deformed geometry and the adapted hydrodynamic influence coefficients based on the calculated structural deformations at each time step. This has been accomplished by constructing new panel files which include the geometry of the deformed blade with the PROPART toolbox [22]. From these new panel files the corresponding hydrodynamic influence coefficients are calculated in PROCAL. Secondly, the source strengths are redefined for each time step with Eq. 5 which includes the blade vibration velocities. Then, a new FSI cycle starts by first computing the steady state solution for the loads from the updated BEM models. When the loads from present and previous FSI cycle differ less than a certain tolerance the fully coupled FSI solution is obtained, otherwise the iterative procedure continues until convergence.



Figure 2: The Nautilus (Photo: H. Huppel).

3. Full-scale composite propeller

This section will describe the most important details of the full-scale propeller and its design. Important to note is that the full-scale composite propeller was not designed for a long lifetime or the demonstration of the benefits of composite ship propellers, but for the validation of the hydroelastic calculation results.

3.1. Vessel and wakefield

The full-scale measurements have been performed on the Nautilus, a diving support vessel of the Royal Dutch Navy, see Figure 2. The main particulars of the vessel are summarized in Table 1. The Nautilus is a twin-screw vessel of which the port-side propeller has been replaced by a composite one. The non-uniform nominal wakefield at the port-side propeller plane has been calculated with a RANS solver for a ship speed of 10 kn. Figure 3 shows the computed wakefield.

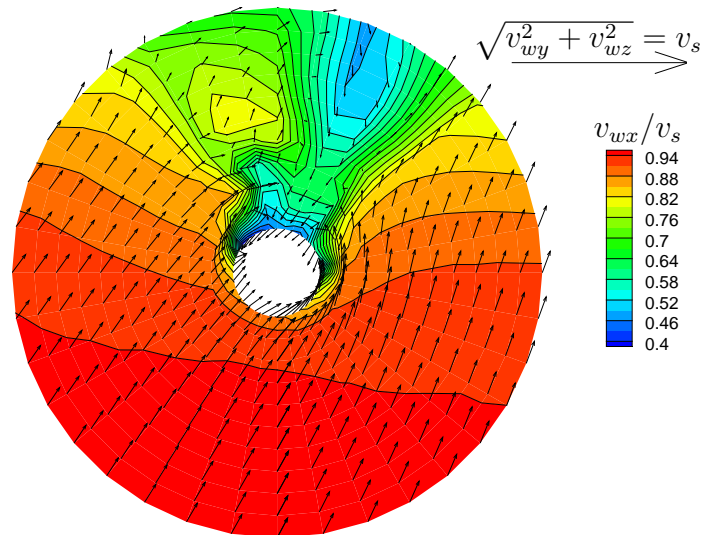


Figure 3: Nominal wakefield at the portside propeller plane of the Nautilus.

Length	37.8 m
Beam	8.7 m
Depth	3.1 m
Draught	1.5 m
Maximum speed	10.5 kn
Propulsion	Twin-screw
Engine	2×Volvo Penta Diesel 280 kW

Table 1: Main particulars of the Nautilus.

3.2. Propeller geometry

In an early design stage it was assessed that the existing blade geometry, Figure 4a, would result in an unacceptable amount of suction side sheet cavitation at higher speeds. Furthermore, to enhance blade flexibility, a propeller geometry with more skew was desired. Therefore, a new propeller geometry, Figure 4b, with a similar open-water performance as the existing blade geometry was designed. The main particulars of the new and old propeller geometry are summarized in Table 2. The main differences between the old and new propeller geometry are in the skew and camber of the propeller section profiles. The change in skew for increasing blade flexibility the change in camber to get rid of the cavitation. Initially, the thicknesses of the composite section profiles were taken similarly to what would have been used in the design of a nickel-aluminium bronze propeller (NAB) propeller, but in a later stage the blade thickness at the root section has been significantly increased to allow for the realisation of the blade-hub connection.

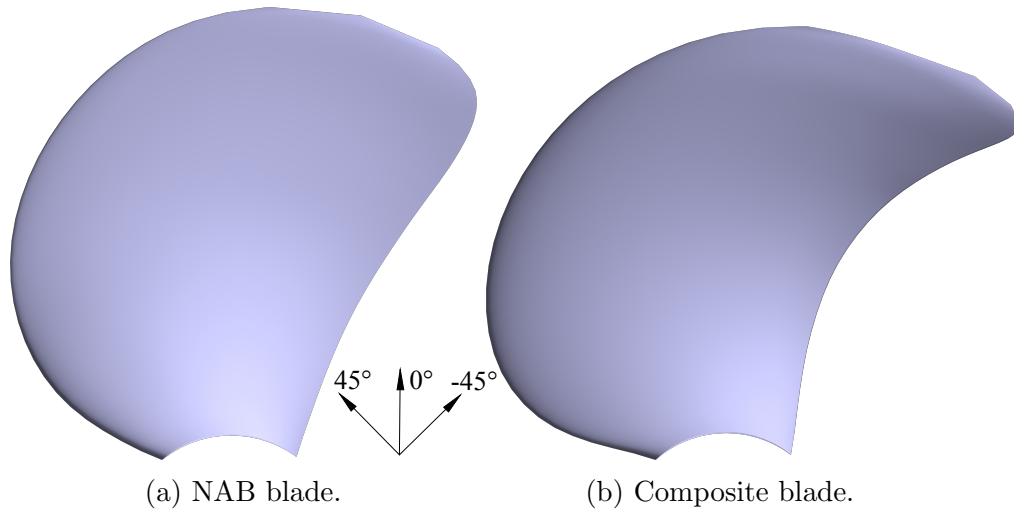


Figure 4: Geometry of NAB and composite blade.

3.3. Propeller structural design

Following the propeller geometry design the propeller structural design was made. The structural design has been based on several considerations, itemized below.

- Since the composite propeller is a retrofit on an existing drive train system, it was most obvious to manufacture separate composite blades and connect the blades to a NAB hub.
- For validation purposes a propeller as flexible as possible was desirable. For that reason glass fibre reinforced epoxy was selected as the blade material.
- General guidelines for the design of layered composites have been adopted. For instance, not more than three plies of equal orientation are stacked together and the maximum angle change between between plies is 45° .
- For blade manufacturing reasons a sandwich construction with an easily compressible resin-rich core material was adopted.

In the structural design process of the composite propeller the connection between composite blades and NAB hub was found to be critical. To create enough space for an appropriate connection, the blade area adjacent

	NAB prop.	Composite prop.
Diameter	1000 mm	1000 mm
Pitch Ratio (mean)	0.94	0.85
Expanded Area Ratio	0.73	0.75
Number of Blades	4	4
Thickness Ratio (mean)	0.0620	0.0817
Camber Ratio (mean)	0.0137	0.0299
Boss Ratio	0.1825	0.1825
Total Skew Angle	29.5°	40.4°
Direction of rotation	outward-turning	outward-turning

Table 2: Main particulars of the original NAB and composite propeller.

to the hub was made significantly thicker than in the initial design. A detailed description of the developed connection is omitted in this work as it is irrelevant to the validation study. In general the connection is of a hybrid type, including an adhesive bonding and a mechanical connection. Both were designed to be able to separately sustain the full load. The strength of the designed blade-hub connection was confirmed by static and fatigue tests on specimens and on full-scale. The glass-epoxy blades have been designed for infinite fatigue life according to the guidelines as given in [23]. The ultimate strength of the blades have been assessed for the two critical loadcases of full speed ahead and full bollard pull astern. It has to be noted that the loads for the first loadcase have been obtained with FSI method as presented before. However, since the BEM PROCAL is not directly applicable to astern conditions the loads for the second loadcase have been computed with a vortex lattice method, excluding the hydro-elastic effects. From these analyses the full bollard pull astern condition turned out to be the most critical, which is not surprising given the high skew of the blades. Since this loadcase was analysed in a simplified way, the propeller was not designed for backward operation and therefore not for long-term use, but for the period of the full-scale trials only. However, from fatigue analyses and tests both the blade-hub connection and blade material itself showed to have an infinite fatigue life. The blades have been produced by a closed mould vacuum assisted resin transfer molding process with a post-cure. For blade manufacturing reasons it was decided to apply a sandwich construction in which a Polymat was

used as a core. The Polymat core has a variable thickness which is 37.5% of the local blade thickness. Advantages of using the Polymat core is that the mould can be more easily closed due to the compressibility of the core material. Secondly, it has good injection properties and therefore it facilitates the vacuum infusion process. The remaining 31.25% of the blade thickness on both blade sides have the same symmetric but unbalanced laminate. The typical stacking sequence of the uni-directional (UD) 0.5 mm thick glass-fibre plies, according to the ply angle definition as given in Figure 4 is, $[20/20/-15/-60/-105/-60/-15/20/20]^\circ$, but can slightly vary due the local thickness. Essentially, this laminate has fibres in three major orientations: -15° , -60° , -105° . The 20° plies have been added to increase the shear-extension coupling. Since the laminate is symmetric the laminate itself has no bend-twist coupling. However, the shear-extension coupling on laminate level creates a bend-twist coupling on a global level in a sandwich structure were the skin laminates are mirror images around the neutral axis [24].

Where the local thickness requires more layers, first 20° plies have been added to increase the shear-extension coupling, then -15° plies and finally -60° plies have been added. Where the local thickness requires a thinner laminate, plies are dropped from inside.

3.3.1. Material properties

The blades consist of the following materials. For the load carrying parts of the blade construction 0.5 mm thick, 600 g/m^2 E-glass UD plies have been used. A Polymat 140 g/m^2 core material with on each side a fiberglass chopped strand mat (CSM) of 1.5 mm thick has been used for the blade core. To protect the blade surfaces a 0.17 mm thick, 200 g/m^2 E-glass woven-roving (WR) ply has been added at the outsides of the laminates. In order to improve the resin flow through the product during injection, between every three to five UD plies, a 0.5 mm thick, $[0/90]^\circ$ woven fabric injection weave (IW) has been added. The corresponding material properties are summarized in Table 3.

	E_{11} [GPa]	E_{22} [GPa]	ν_{12} [-]	G_{12} [GPa]	ρ [kg/m ³]
E-glass UD	34.6	5	0.30	3.1	1.8
E-glass WR	21.6	21.6	0.19	3.0	1.8
E-glass IW	10.1	10.1	0.23	2.5	1.4
Polymat	3.50	3.50	0.36	1.4	1.2
CSM	10.4	10.4	0.34	4.0	1.6

Table 3: The (in-plane) material properties of the composite propeller constituents.

3.4. FEM modelling of the full-scale propeller

For FEM modelling and computations MSCMarc/Mentat has been used. The FEM model of the full-scale propeller consists of one propeller blade without the hub part. The hub has not been modelled. The blade has been fully clamped at the blade-hub interface. The models were discretised by quadratic solid elements. Layered quadratic solid elements have been used, the complete stacking sequence was modelled by including each individual layer in the FEM model. A structured FEM mesh has been used with a $29 \times 30 \times 4$ element distribution, meaning that 29, 30 and 4 elements are distributed in chord-wise, radial and through-thickness direction, respectively. In the FEM modelling special attention has been given to the establishment of the material orientations in composite blades. In [19, 25] the importance of a proper material orientations for doubly curved structures has been described. Standard commercial FEM software packages are usually not able to define unambiguously the material orientations in complex geometries [25]. In [19] an approach has been presented to determine the element dependent material orientations in doubly curved structures. In this method the through thickness direction and the projection of the transverse laminate (90)-direction on the element surface is used to establish the material orientation per element. A more detailed description of this approach and the blade FEM modelling can be found in that paper.

3.4.1. Verification

The FEM model of the full-scale propeller has been verified by comparing measured and computed dry natural frequencies and mode shapes. The dry natural frequencies and mode shapes of the full-scale propeller have been measured during a roving hammer test. A grid on the surface of all the propeller blades was drawn, in each grid point the blades were hit with

the hammer and the response was measured at the propeller tip with an accelerometer. Two of the pictures made during the tests are shown in Figure 5.

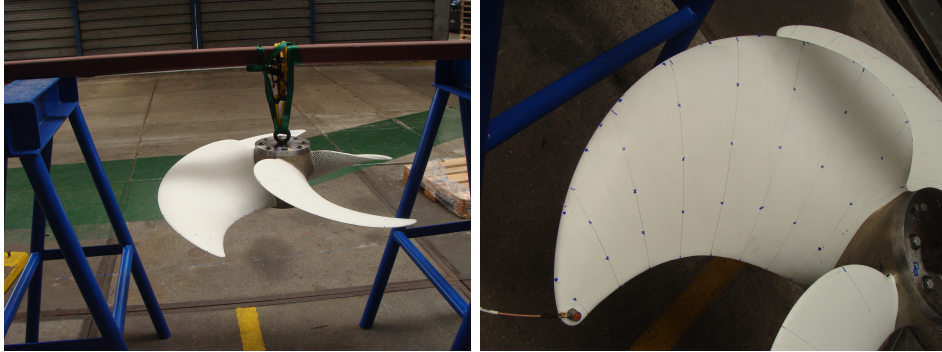


Figure 5: Images taken during the natural frequency measurements of the composite blades.

Table 4 presents the measured and computed dry natural frequencies for the first four modes. It can be concluded that the computed and measured dry natural frequencies are close together. Furthermore, the weights of the separate blades have been measured and checked with the amount of mass in the FEM calculation. The weight of the blades as measured and in the FEM calculation is approximately 4 kg. Hence, it can be concluded that the FEM model correctly represents the mass and stiffness distribution of the propeller blades.

	mode 1 [Hz]	mode 2 [Hz]	mode 3 [Hz]	mode 4 [Hz]
Measured	119	188	339	430
Computed	114	186	316	435

Table 4: Measured and computed natural frequencies.

4. Full-scale measurements

4.1. Measurement technique

Stereo-photography coupled with a Digital Image Correlation (DIC) technique was selected to measure the propeller blade deformations. With this technique a very accurate recording of the complete 3D blade deformation

field can be achieved. In the past, this method was successfully applied for blade deformation measurements both in uniform flow in the cavitation tunnel and in-behind ship model condition in the towing tank [26, 27].

DIC is a full-field image analysis method, based on grey value digital images that finds the displacements and deformations of an object in three dimensional space [28]. The method tracks the gray value pattern in pixel subsets of the images and computes the three-dimensional deformation pattern through the stereoscopic principle. The surface of the specimen must present a random speckle pattern with no preferred orientation and sufficiently high contrast. On the pressure side of the blades a hand-painted speckle pattern was applied. With this technique very accurate measurements of the blade response were achieved.

4.2. Measurement set-up

The development of the measurement set-up was a complex process due to the uniqueness of such measurement campaign. A feasibility study was conducted at an early stage to investigate the possibilities for measuring the propeller deflections on full-scale where several options were studied. It was concluded that under water stereo-photography presented the most chance of success for this specific case. This approach required several additional tests to assess the feasibility of this measurement technique at the preferred test location and time as the underwater visibility may vary during the year due to algae blooms. The result of the assessment was positive as the water visibility was found excellent [29]. Due to the fast rotational speed of the propeller and the limited amount of natural light available under the ship hull, it was also concluded that a large amount of artificial light was necessary to avoid motion blur. Another challenge was to find the best position for the cameras. It was decided to position the cameras on the rudder, which resulted in additional challenges for the routing of the cables due to rudder movements and the strong flow at this location.

After performing the pre-study the measurement set-up was further detailed out including: the camera set-up, a custom made remote control of the optics and a custom made underwater strobe illumination system. Since no underwater cameras with the right specification were available, two high quality machine vision cameras have been used, protected by underwater housings. The cameras were triggered through a hardware pulse synchronized with the propeller shaft. A support structure for the camera housings was developed, consisting of a base plate welded on the rudder and an L-bar mounted to the

base plate (Figure 6). The L-bar has slot holes for adjustment of the camera view after assembly. The cameras were positioned for an optimal view at the propeller blade in the twelve o'clock position. Further, a custom made remote control of the optics was developed in order to optimise the lens focus and aperture from on-board.

For the underwater illumination as a first step, off the shelf underwater lights were assessed, but no items, able to provide sufficient light intensity while being reasonably compact, were found. The solution was found by developing small custom made subsea strobe lights triggered by a hardware pulse, synchronized with the propeller shaft and the cameras. Two sets of 4 lights were prepared and mounted respectively on the rudder and on the hull approximately 1 m to portside of the rudder stock (Figure 7).



Figure 6: Starboard rudder side with cameras.



Figure 7: Lights on rudder and hull and cables.

4.3. *The measurements*

The measurements were carried out October 31st and November 1st, 2017. Two stereo images taken with both cameras for the highest rotation rate are shown in Figure 8. During all the tests, ship speed, distance and heading, and on both shafts the rotation rate and with strain gauges the torque were measured. Tests were conducted at different propeller speeds, sailing on both propellers, but also only on the portside composite propeller. The reason was that for higher speeds a large amount of air bubbles obstructed the view when sailing on both propellers. With only the composite propeller running, a drift angle was induced which reduced the amount of air bubbles in the image plane. For each test a large amount of images were taken and image averaging was applied to filter out displacements resulting from transient behaviour and to remove air bubbles and particles from the images. The results were further post-processed and a procedure was applied to correct for rigid body motions induced by vibrations and movements of the shaft and the rudder. While the measurement data of the highest quality was collected when sailing with only the portside propeller running, a fair comparison to the numerical results for these conditions would require a recalculation of the wake field including the effect of the drift angle. This activity was not carried out as part of this research work, therefore the related uncertainties lead to a worse match between numerical and experimental results for the

cases with only the portside propeller running. More details on the full-scale measurement campaign can be found in [29].

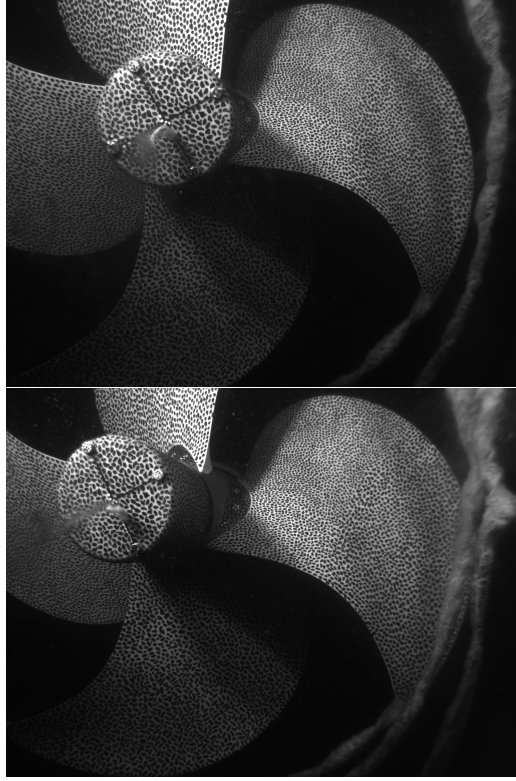


Figure 8: Stereo images for the maximum rotation rate (Photos: MARIN).

5. Comparison of experimental and calculation results

5.1. Test conditions and torque results

Although the measurement data of the highest quality was collected when sailing only on the portside propeller, from a comparison of numerical and experimental results it turned out that the best resemblance between calculation and measurement results has been obtained for the conditions with both propellers in operation. This is not surprising, because due to drifting of the vessel the propeller inflow in the cases of sailing on one propeller will become significantly different from the RANS computed wakefield. Therefore, a fair comparison to the numerical results for these conditions would require a recalculation of the wakefield including the effect of the drift angle.

This activity was not carried out as part of this research work. For that reason only results will be presented for the conditions with both propellers in operation. For these conditions measurements have been conducted for the ship speeds and rotation rates of Table 5. This table presents also the measured torque of the portside composite propeller and the torque computed for the composite propeller and for the assumed completely rigid starboard propeller. The results show that the flexible properties of the composite propeller reduces the torque by approximately 5%. The results also reveal that the measured torque is more than 15% higher than calculated. These differences are attributed to using the nominal wakefield for the calculations instead of the effective wakefields.

	Ship speed [kn]	Rotation rate [rpm]	PS measured torque [kNm]	Calculated torque	
				PS [kNm]	SB [kNm]
Blade 7, low load, twelve o'clock	7.7	420	2.14	1.84	1.92
Blade 7, high load, twelve o'clock	9.0	473	2.72	2.26	2.38
Blade 8, low load twelve o'clock	7.7	411	2.06	1.73	1.81
Blade 8, high load twelve o'clock	8.7	466	2.61	2.23	2.34
Blade 7, low load, one o'clock	8.1	421	2.11	1.78	1.88
Blade 7, high load, one o'clock	8.8	468	2.74	2.21	2.34
Blade 7, low load, half past two	8.2	419	2.10	1.74	1.84
Blade 7, high load, half past two	8.8	471	2.65	2.25	2.38

Table 5: Test conditions, measured torque results portside (PS) composite propeller and calculated torque results for PS composite and starboard (SB) rigid propeller.

5.2. Uncertainties

For uniform flow experiments and calculations on model-scale, an uncertainty estimation has been presented in [20]. From this study it was concluded that the discretisation errors in the BEM-FEM calculations can be assumed negligible compared to modelling uncertainties due to not exactly modelling the properties and conditions as appearing in the experiments. For these class of errors the two most important sources were using the design propeller geometry and the design elastic properties instead of the as-built geometry and actual elastic properties. It is assumed for this work that the error due to differences between design and actual geometry will be negligibly small, because of the improved procedure for the assembly of blades and hub. The results of the natural frequency tests indicate that the FEM model correctly represents the mass and stiffness distribution of the propeller blades, therefore as stiffness modelling error only $\pm 5\%$ has been assumed. The largest modelling error, which is not present in uniform flow experiments, is expected to be in the wakefield. First, the RANS computed nominal wakefield has been used for the calculations instead of the effective wakefield. Secondly, this wakefield has been computed for a ship speed of 10 kn and has been used for other conditions as well. Thirdly, as advance velocity the ship speed has been used, which would be true in laboratory conditions, however in full-scale measurements the advance velocity may be influenced by waves, current and drift angle. It has been considered outside the scope of this work to define how large the wakefield uncertainties are. However, given the differences between measured and computed torque as can be seen in Table 5, significant differences between the RANS computed nominal wakefield and actual propeller inflow can be expected. In order to correct for this, the whole pressure distributions calculated with the BEM have been amplified evenly with the ratio between the measured torque and the uncorrected calculated torque as given in Table 5 in order to have identical torque in measurements and calculations in the end. The remaining modelling uncertainty (including the $\pm 5\%$ stiffness uncertainty) has been assumed to be $\pm 10\%$ on bend and twist deformations.

For the DIC measurements an uncertainty of ± 0.25 mm has been assumed. This value is based on the measurement noise as observed in the data and the consideration that the measured blade response adjacent to the hub should be zero, which is generally not the case. With the calculation rules for uncertainties the twist deformation uncertainty could be obtained from the displacement uncertainty.

5.3. Comparison of computed and measured blade response

Figure 9 shows the calculated and measured bend and twist deformations at the mid-chord points against the radial position, for the low and high load, for blade 7 and 8 in the twelve o'clock position. Results for both blades have been shown in the same figure in order to compare them. The graphs show that the responses of both blades are very similar. This was already expected from the results of the natural frequency tests. Since the results for blade 7 and 8 are similar, only results for blade 7 will be shown.

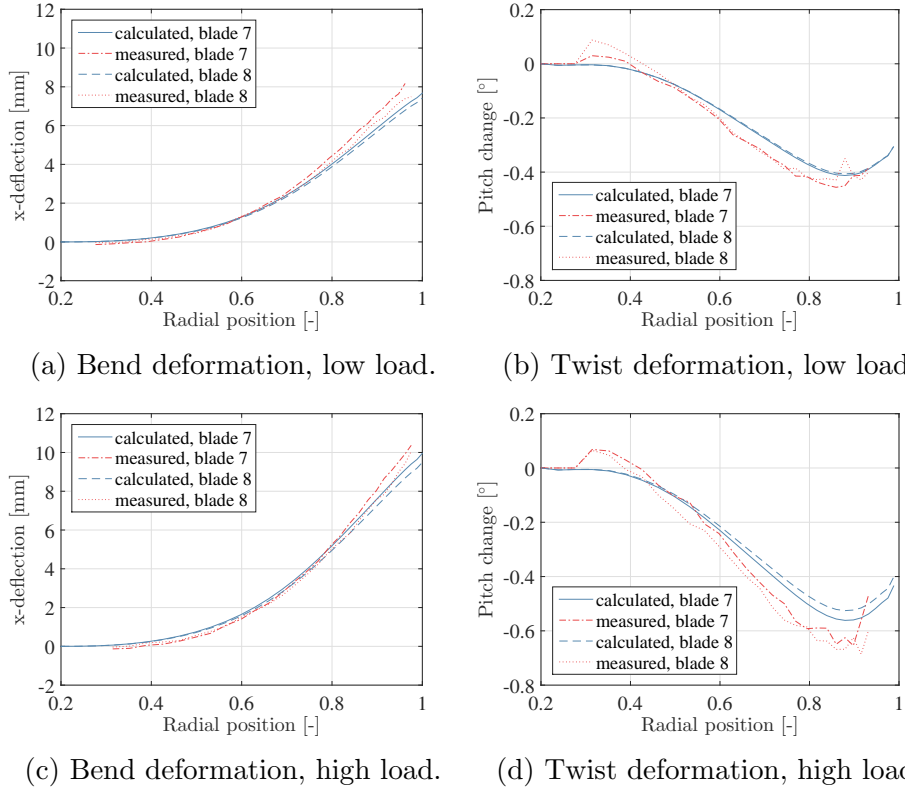
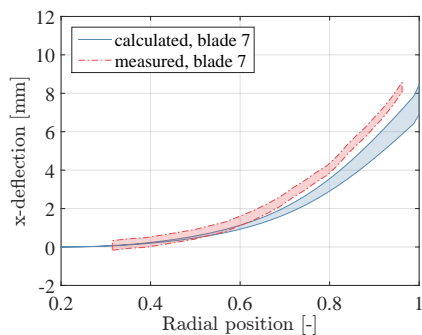


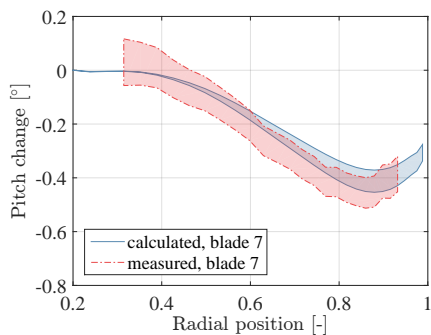
Figure 9: Calculated and measured bend (left) and twist (right) deformations of the mid-chord points against the radial position, for blade 7 and 8 in the twelve o'clock position.

Figures 10 to 12 show the uncertainty intervals for measured and calculated bend and twist deformations against the radial position, for the low and high load for blade 7 in the twelve o'clock, one o'clock and half past two position. The uncertainty intervals for the numerical results have been obtained from the BEM-FEM calculations with amplified pressures for torque identity and assuming $\pm 10\%$ uncertainty in the obtained bend and twist deformations. The uncertainty interval for the bend deformations is the ± 0.25 mm bandwidth around the measured displacements. The uncertainty interval for the measured twist deformations has been computed with the calculation rules for uncertainties from the ± 0.25 mm uncertainty in the displacements. Figures 10 to 12 show a very good resemblance between calculated and measured bend deformations. The BEM-FEM calculation slightly underestimates the bend deformation for the twelve o'clock and half past two position. The opposite is the case for the one o'clock position. A

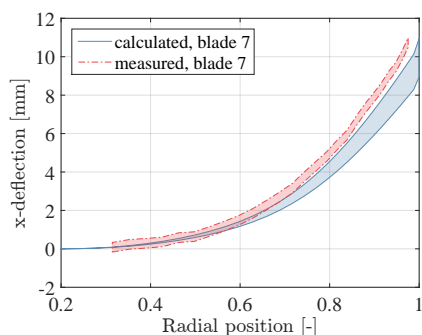
good resemblance between calculated and measured twist response has been obtained for the twelve o'clock position. For the two other blade positions the resemblance is less good, especially for the half past two position. Given its magnitude, the measurement of blade twist is strongly correlated with the measurement uncertainty. The measurement system was optimised for the twelve o'clock position, therefore the light conditions on the blade surface for the one o'clock and two o'clock positions are sub-optimal, especially in the tip area. This may explain why the twist comparison is shown less accurate in the high radii location for these cases. Furthermore, for the half past two position the larger deviation in measured and calculated twist response is also due to difficulties in applying the rigid body motion correction.



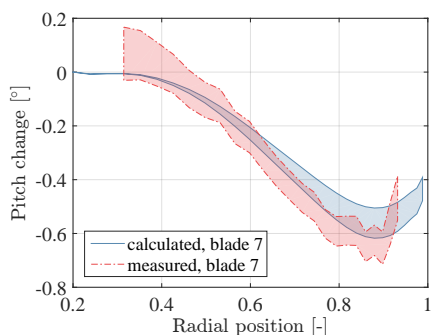
(a) Bend deformation, low load.



(b) Twist deformation, low load.

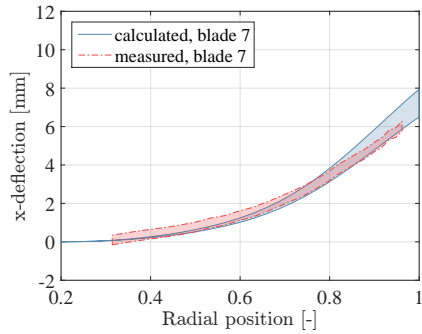


(c) Bend deformation, high load.

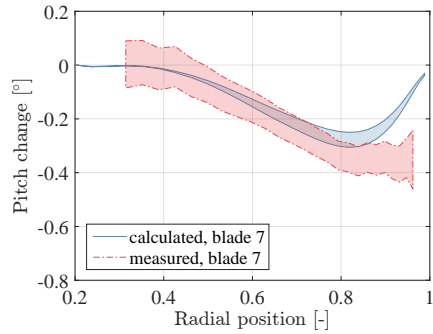


(d) Twist deformation, high load.

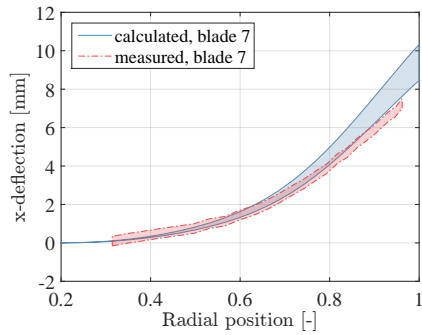
Figure 10: Calculated and measured bend (left) and twist (right) deformations of the mid-chord points against the radial position, for blade 7 in the twelve o'clock position.



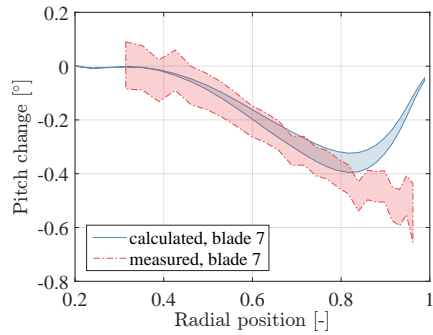
(a) Bend deformation, low load.



(b) Twist deformation, low load.

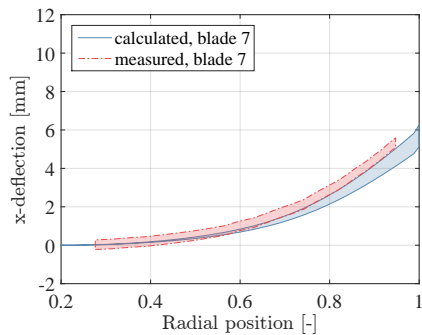


(c) Bend deformation, high load.

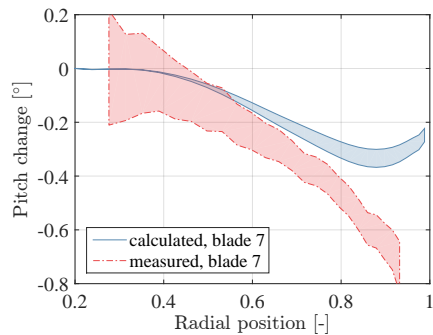


(d) Twist deformation, high load.

Figure 11: Calculated and measured bend (left) and twist (right) deformations of the mid-chord points against the radial position, for blade 7 in the one o'clock position.



(a) Bend deformation, low load.



(b) Twist deformation, low load.

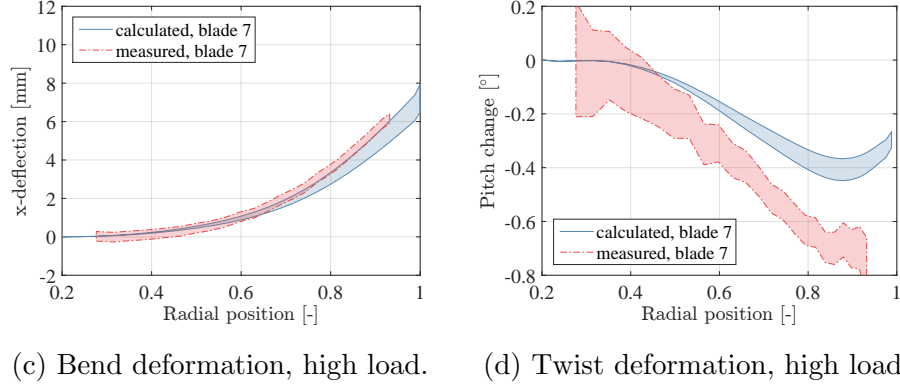


Figure 12: Calculated and measured bend (left) and twist (right) deformations of the mid-chord points against the radial position, for blade 7 in the half past two position.

6. Conclusions

A partitioned FSI coupling for the non-uniform flow hydro-elastic analysis of highly flexible propellers in cavitating and non-cavitating conditions has been presented. The method is a partitioned FSI method in which coupling iterations between fluid and structural solver are performed on a periodic level rather than per time step in order to accomplish the strong coupling between the fluid and structural sub-domain. A time periodic coupling was necessary for the present BEM-FEM coupling, since the BEM method is completely periodical in nature and therefore a time step coupling would not converge. In addition, a time periodic coupling allows to solve the structural problem in the frequency domain, which is advantageous for the convergence speed. In the BEM-FEM coupling procedure the structural sub-problem has been solved in the frequency domain, in wet modal space, which allows for a model reduction by involving only a limited number of mode shapes. The present FSI framework is not confined to this way of solving the structural equations. For instance, it would be also possible to include a geometrically non-linear FEM, because of the full separation of fluid and structural solver. From the validation study on full-scale the following conclusions can be drawn:

- The comparison between measured and computed natural frequencies confirms that the FEM modelling is fairly accurate.

- The measurement of the blade deflections were successfully carried out at full-scale with a stereo-camera system coupled with a DIC technique.
- The comparison between measured and calculated blade responses shows that the blade response is well predicted with the BEM-FEM coupling for non-uniform flows.
- The results show that the twist response is relatively small and the uncertainty in the twist response is relatively large. It remains a challenge to obtain accurately the twist response of flexible blades with a stereo camera measurement set-up in combination with a DIC technique, which is a point of attention for the future.

7. Acknowledgements

The authors gratefully acknowledge the Defence Materiel Organisation, Maritime Research Institute Netherlands, Wärtsilä Netherlands B.V., Solico B.V. and NWO, domain Toegepaste en Technische Wetenschappen (project number 13278) for their financial support. The authors would gratefully thank the Cooperative Research Ships (CRS) for making their BEM software PROCAL available for this work. The authors would gratefully acknowledge Maritime Research Institute Netherlands for making their propeller geometry toolbox PROPART available for this work. The authors gratefully thank Royal Netherlands Navy for making the Nautilus available for the sea trials.

- [1] H. Lee, M. Song, J. Suh, B. Chang, Hydro-elastic analysis of marine propellers based on a bem-fem coupled fsi algorithm, *International Journal of Naval Architecture and Ocean Engineering* 6 (2014) 562–577.
- [2] X. He, Y. Hong, W. RG., Hydro-elastic optimisation of a composite marine propeller in a non-uniform wake, *Ocean Engineering* 39 (2012) 1423.
- [3] Y. Young, Time-dependent hydro-elastic analysis of cavitating propulsors, *Journal of Fluids and Structures* 23 (2007) 269–295.
- [4] L. Jiasheng, Q. Yegao, H. Hongxing, Hydroelastic analysis of underwater rotating elastic marine propellers by using a coupled bem-fem algorithm, *Ocean Engineering* 146 (1) (2017) 178–191.

- [5] P. Maljaars, M. Kaminski, den Besten JH., Boundary element modelling aspects for the hydro-elastic analysis of flexible marine propellers, *Journal of Marine Science and Engineering* 6 (2).
- [6] E. van Brummelen, Partitioned iterative solution methods for fluid-structure interaction, *International Journal for Numerical Methods in Fluids* 65 (1-3) (2011) 3–27.
- [7] E. van Brummelen, Added mass effects of compressible and incompressible flows in fluid-structure interaction, *Journal of Applied Mechanics* 76 (2) (2009) 021206–7.
- [8] Y. Young, M. Motley, R. Barber, E. Chae, N. Garg, Adaptive composite marine propulsors and turbines: Progress and challenges, *Applied Mechanics Reviews* 68 (6) (2016) 060803.
- [9] G. Vaz, Modelling of sheet cavitation on hydrofoils and marine propellers using boundary element methods, Ph.D. thesis, Instituto Superior Técnico, Lisbon, Portugal (2005).
- [10] G. Vaz, J. Bosschers, Modelling of three dimensional sheet cavitation on marine propellers using a boundary element method, *Sixth International Symposium on Cavitation*, Wageningen, The Netherlands, 2006.
- [11] E. van den Bunt, W. Lafeber, Optical measurement techniques in model testing, *Advanced Model Measurement Technology*, Newcastle, England, 2011.
- [12] T. Taketani, K. Kimura, A. S., K. Yamamoto, Study on performance of a ship propeller using a composite material, *Third International Symposium on Marine Propulsors*, Launceston, Tasmania, Australia, 2013.
- [13] L. Savio, Measurements of the deflection of a flexible propeller blade by means of stereo imaging, *Fourth International Symposium on Marine Propulsors*, Austin, Texas, USA, 2015.
- [14] P. Maljaars, J. Dekker, Hydro-elastic analysis of flexible marine propellers, in: C. Guedes Soares, T. Santos (Eds.), *Maritime Technology and Engineering*, 2014, pp. 705–715.

- [15] B. Chen, S. Neely, T. Michael, S. Gowing, R. Szwer, D. Buchler, R. Schult, Design fabrication and testing of pitch-adapting (flexible) composite propellers, The SNAME Propeller/Shafting Symposium, Williamsburg, VA, USA, 2006.
- [16] P. Maljaars, M. Kaminski, den Besten JH., A new approach for computing the steady state fluid-structure interaction response of periodic problems, *Journal of Fluids and Structures* 84 (2018) 140–152.
- [17] J. Degroote, R. Haelterman, S. Annerel, P. Bruggeman, J. Vierendeels, Performance of partitioned procedures in fluidstructure interaction, *Computers Structures* 88 (78) (2010) 446–457.
- [18] L. Morino, C. Kuo, Subsonic potential aerodynamics for complex configurations: a general theory, *AIAA Journal* 12 (2) (1974) 191197.
- [19] P. Maljaars, M. Kaminski, J. den Besten, Finite element modelling and model updating of small scale composite propellers, *Composite Structures* 176 (2017) 154–163.
- [20] P. Maljaars, L. Bronswijk, J. Windt, N. Grasso, M. Kaminski, Experimental validation of fluid-structure interaction computations of flexible composite propellers in open water conditions using bem-fem and rans-fem methods, *Journal of Marine Science and Engineering* 6 (2).
- [21] T. Scholcz, Multi-fidelity methods for fluid-structure interaction and uncertainty quantification, Ph.D. thesis, Delft University of Technology, Delft, The Netherlands (2015).
- [22] J. Huisman, E. Foeth, Automated multi-objective optimization of ship propellers, Fifth International Symposium on Marine Propulsors, Espoo, Finland, 2017.
- [23] Germanischer Lloyd, Guideline for the certification of Wind Turbines, Chapter 5.5 (2010).
- [24] W. de Goeij, M. van Tooren, A. Beukers, Implementation of bending-torsion coupling in the design of a wind-turbine rotor-blade, *Applied Energy* 63 (3) (199) 191–207.

- [25] J. Chen, S. Hallet, M. Wisnom, Modelling complex geometry using solid finite element meshes with correct composite material orientations, *Computers and Structures* 88 (2010) 602–609.
- [26] G. Zondervan, N. Grasso, W. Lafeber, Hydrodynamic design and model testing techniques for composite ship propellers, Fifth international symposium on marine propulsion, Espoo, Finland, 2017.
- [27] P. Maljaars, N. Grasso, M. Kaminski, W. Lafeber, Validation of a steady bem-fem coupled simulation with experiments on flexible small scale propellers, Fifth international symposium on marine propulsion, Espoo, Finland, 2017.
- [28] J. Sutton, J. Ortue, H. Schreier, *Image Correlation for Shape, Motion and Deformation Measurements: Basic Concepts, Theory and Applications*, Springer, New York, 2009.
- [29] N. Grasso, R. Hallmann, T. Scholcz, G. Zondervan, R. Schouten, P. Maljaars, Experimental investigations of the hydro-elastic behaviour of flexible composite propellers in non-uniform flow at model and full scale (in preperation), Sixth International Symposium on Marine Propulsors, Rome, Italy, 2019.